Research Square

Preprints are preliminary reports that have not undergone peer review.
They should not be considered conclusive, used to inform clinical practice,
or referenced by the media as validated information.

Experimental study of flame characteristics of methane diffusion combustion with metal fiber burner under O_2/CO_2 oxy-fuel

Yujie Lin

linyj.qday@sinopec.com

State Key Laboratory of Chemical Safety

Chang Qi

State Key Laboratory of Chemical Safety

Chen Kuang

State Key Laboratory of Chemical Safety

Guanlin Peng

State Key Laboratory of Chemical Safety

Research Article

Keywords: Oxy-fuel combustion, O_2/CO_2 atmosphere, metal fiber burner, Methane diffusion flame, CO burnout

Posted Date: November 12th, 2026

DOI: https://doi.org/10.21203/rs.3.rs-11531071/v1

License: This work is licensed under a Creative Commons Attribution 4.0 International License.
Read Full License

Additional Declarations: No competing interests reported.

Experimental study of flame characteristics of methane diffusion combustion with metal fiber burner under O_2/CO_2 oxy-fuel

Yujie Lin [a,b.c] *, Chang Qi [a,b.c], Chen Kuang [a,b.c],Guanlin Peng [a,b.c]

[a] State Key Laboratory of Chemical Safety, Qingdao, Shandong 266000, China

[b] SINOPEC Research Institute of Safety Engineering Co. Ltd., Qingdao, Shandong 266000, China

[c] National Registration Center for Chemicals, Ministry of Emergency Management, Qingdao, Shandong 266000, China

*Corresponding author: Yujie Lin (linyj.qday@sinopec.com)

Abstract

O_2/CO_2 oxy-fuel combustion can produce CO_2-rich flue gas and suppress nitrogen-oxide formation, but the high heat capacity, infrared activity, and chemical participation of CO_2 can simultaneously alter flame stabilization and CO burnout. Methane free diffusion flames and flames formed around a vertical cylindrical metal fiber burner were therefore examined in an O_2/CO_2 coflow under identical operating boundaries. The total coflow rate was fixed at 20 L/min, the oxygen mole fraction was varied from 21% to 35%, and the methane flow rate was 5-20 L/min. Visible and infrared imaging, fixed-height thermocouple measurements, radiative heat-flux measurements, and dry-basis CO/NOx analysis were combined to establish a structure-thermal-radiation-emission relationship. The metal fiber burner redistributed methane through its porous sidewall and formed a coupled near-wall surface-combustion region and upper thermal plume. At high load, the 13-29 cm region approached approximately 800 °C. Radiative heat flux was controlled mainly by methane flow rate, increasing from about 35-50 W/m^2 at 5 L/min to 240-300 W/m^2 at 20 L/min. Oxygen enrichment promoted CO post-oxidation: for the metal fiber burner, CO decreased from approximately 315 to 240 ppm at 5 L/min and from 165 to 45 ppm at 10 L/min. At 15-20 L/min, CO fell to roughly 7-31 ppm. NOx remained approximately 1.5-4.8 ppm across most conditions. The results identify low-load CO burnout, rather than NOx, as the principal operating constraint for CO_2-diluted metal fiber combustion and provide quantitative guidance for low-NOx, carbon-capture-compatible burner design.

Keywords: Oxy-fuel combustion; O_2/CO_2 atmosphere; metal fiber burner; Methane diffusion flame; CO burnout

1. Introduction

Methane is the principal constituent of natural gas and remains a major fuel for refinery furnaces, boilers, radiant heaters, and compact process-heating units. Decarbonizing these systems requires not only higher conversion efficiency but also flue-gas configurations that are compatible with CO_2 capture. Conventional air combustion introduces a large nitrogen ballast, which increases exhaust volume, carries sensible heat from the combustion chamber, dilutes CO_2, and creates the molecular-nitrogen reservoir for thermal NO formation. Oxy-fuel combustion replaces most or all of this nitrogen with recycled CO_2 or another controlled diluent and can therefore produce a concentrated CO_2/H_2O exhaust stream suitable for downstream purification and capture [1-4].

The term oxy-fuel combustion does not imply that the diluent is chemically neutral. CO_2 has a higher molar heat capacity than N_2 over the relevant temperature range, is strongly active in the infrared, and interacts with the hydrogen-radical pool through reactions such as $CO_2 + H \rightleftharpoons CO + OH$. As a result, CO_2 affects adiabatic temperature, flame speed, stabilization, soot luminosity, CO post-oxidation, and gas radiation simultaneously [5-11]. Recent work on methane and syngas oxy-flames has shown that oxygen fraction, coflow temperature, dilution level, and burner aerodynamics cannot be treated independently; they determine the location and volume of the high-temperature zone and therefore the balance among burnout, thermal radiation, and NOx formation [4-9].

For non-premixed methane flames, the effect of CO_2 is particularly important because oxidation is mixing controlled and CO is formed and consumed over spatially separated regions. Kim et al. [8] showed that oxygen concentration in an O_2/CO_2 coflow strongly affects the stability and visible structure of non-premixed coaxial flames. Glarborg and

Bentzen [9] demonstrated that high CO_2 levels alter methane chemistry beyond a purely thermal effect, while Chen et al. [10] quantified the uncoupled chemical and thermal effects of CO_2 on CH_4/O_2 counterflow diffusion flames. These observations explain why a flame can exhibit a locally high measured temperature yet retain significant CO if the post-flame zone lacks sufficient OH, oxygen, or residence time.

Radiative heat transfer is another defining feature of CO_2-rich combustion [12,13]. CO_2 and H_2O are participating media, so a decrease in visible luminosity does not necessarily imply a proportionate decrease in total radiation. Plasma-assisted biogas experiments have confirmed that CO_2 dilution changes both luminescence and thermal-radiation signatures [12], and laboratory combustor studies indicate that diluent properties alter dynamic response as well as mean temperature [13]. Consequently, burner design for oxy-fuel service must consider the spatial distribution of radiating gases, not only peak flame temperature.

Burner structure provides an additional means of controlling these competing effects. Porous-media and metal fiber burners distribute reactants over a large surface, promote gas-solid heat exchange, and can recirculate heat to the incoming mixture [14-19]. Metal fiber surfaces are especially attractive for compact heating because FeCrAl-based matrices combine high-temperature oxidation resistance, thermal conductivity, permeability, and radiative capability. Recent investigations have quantified the effects of fiber porosity, hydrogen enrichment, fuel loading, and combustion mode on stability and emissions [17-24]. Efficient chemiluminescence-based characterization of metal fiber burners has also emphasized the strong coupling between surface temperature, flame mode, and pollutant formation [20].

Most published metal fiber studies concern fully premixed surface flames. The present configuration differs fundamentally: methane enters the interior of a sealed cylindrical

element, diffuses radially through the fibrous sidewall, and reacts with an external O_2/CO_2 coflow. The fuel boundary condition therefore changes from a central jet to a distributed porous surface. A free diffusion flame operated with the same nozzle and coflow provides a reference for separating the effects of porous redistribution and solid heat feedback. Similar recent porous-burner research has shown that oxy-methane stabilization, pore-scale transport, and volume-averaged modeling all remain sensitive to geometry and thermal non-equilibrium [25-27].

Three gaps motivate this study. First, quantitative data are limited for diffusion-mode metal fiber combustion under CO_2-diluted oxy-fuel conditions. Second, flame images, fixed-height temperatures, radiative heat flux, and emissions are often considered separately, although they represent sequential manifestations of the same combustion process. Third, the operating constraint at low load is not established: a heated metal matrix can stabilize a surface flame, but it can also remove heat from a weak reaction zone and inhibit CO burnout. Combustion-safety studies further demonstrate that oxidizer composition and thermal conditions can shift operational boundaries, reinforcing the need for experimentally defined limits [28-30].

Accordingly, methane free diffusion flames and cylindrical metal fiber burner flames were tested in an O_2/CO_2 coflow over methane flow rates of 5-20 L/min and oxygen mole fractions of 21-35%. The present study: (i) characterizes visible and infrared flame evolution, (ii) quantifies the temperature and radiative response at fixed measurement positions, (iii) resolves the load- and oxygen-dependent CO/NOx behavior, and (iv) develops a structure-thermal-radiation-emission framework for defining an engineering operating window.

2. Experimental setup and methodology

2.1 Experimental system and combustion configurations

The experimental system comprised a methane supply, an automatic oxidizer distribution system, four coflow ports, a vertical test frame, a flue-gas collection hood, optical diagnostics, temperature and heat-flux sensors, and an industrial gas analyzer. Fig. 1 shows the apparatus and the cylindrical metal fiber burner. Methane of 99.99% purity was supplied from below. The O_2/CO_2 oxidizer was premixed to the target oxygen mole fraction and delivered through four 6 mm ports arranged around the central burner. The total coflow rate was fixed at 20 L/min for every condition, thereby avoiding a change in coflow momentum when oxygen fraction was varied.

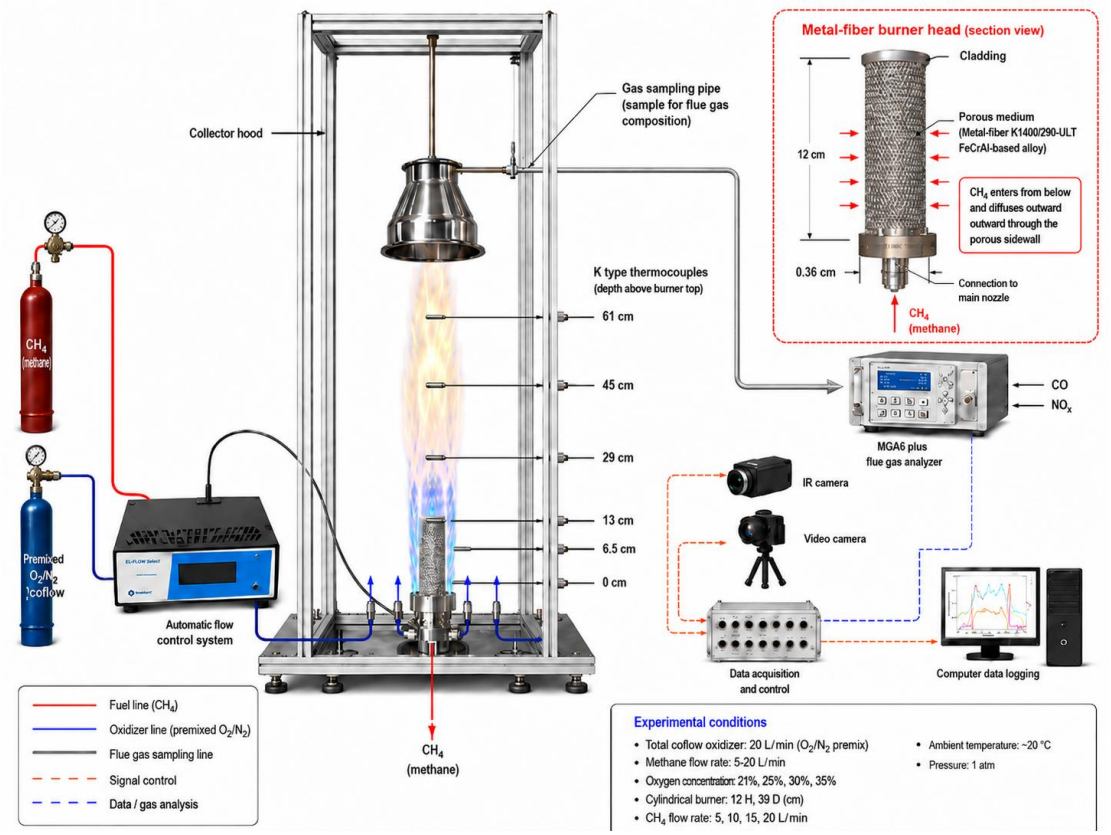


Fig. 1. Experimental system, diagnostic layout, and section view of the cylindrical metal fiber burner.

Two combustion configurations were examined. In the free diffusion configuration, methane exited vertically through the 39 mm inner-diameter main nozzle and mixed with the surrounding O_2/CO_2 coflow. In the metal fiber configuration, the same methane stream entered a vertical cylindrical burner attached to the nozzle. The cylinder was 12 cm high and 39 mm in diameter, its top was sealed, and its sidewall was made from a permeable metal fiber layer. Methane therefore diffused radially through the sidewall and formed a surface-supported reaction region before the products developed into an upper plume. The principal geometric and operating parameters are summarized in Table 1.

Table 1. Main experimental parameters.

Item	Parameter or setting
Fuel	Methane, 99.99% purity
Combustion configurations	Free diffusion flame; cylindrical metal fiber burner flame
Main nozzle inner diameter	39 mm
Metal fiber burner	Vertical cylinder, 12 cm high and 39 mm diameter; closed top; fibrous sidewall
Coflow oxidizer	Premixed O_2/CO_2
Oxygen mole fractions	21%, 25%, 30%, and 35%
Methane flow rates	5, 10, 15, and 20 L/min
Total coflow rate	20 L/min
Ambient conditions	Approximately 20 °C and 1 atm

2.2 Metal fiber material

The burner sidewall was fabricated from K1400/290-ULT metal fiber material. It is a knitted short-fiber FeCrAl-based alloy containing Y, Hf, and Zr. The material provides a stable porous fuel-distribution surface and remains suitable for repeated heating below its stated maximum service temperature. Its nominal properties are summarized in Table 2.

Table 2. Nominal properties of the metal fiber material.

Property	Value or description
Product type	K1400/290-ULT
Base material	FeCrAl alloy containing Y, Hf, and Zr
Fiber form	Short fiber / knitted structure
Surface density	1400 ± 100 g/m²
Permeability	2900 ± 300 L/(m²·s)
Thickness	≥1.8 mm
Maximum service temperature	1100 °C

2.3 Operating matrix

The operating matrix contained one oxidizer atmosphere, two burner configurations, four methane flow rates, and four oxygen fractions, giving 32 base conditions. Each condition was maintained until the visible flame, thermocouple signal, heat-flux signal, and analyzer readings were stable. The matrix is listed in Table 3.

Table 3. Operating matrix for O_2/CO_2 methane combustion.

Variable	Levels or setting
Coflow atmosphere	O_2/CO_2
Combustion configuration	Free diffusion flame; cylindrical metal fiber burner

Methane flow rate	5, 10, 15, and 20 L/min
Oxygen mole fraction	21%, 25%, 30%, and 35%
Coflow ports	Four ports, each 6 mm in diameter
Total coflow rate	20 L/min
Number of base conditions	$1 \times 2 \times 4 \times 4 = 32$

2.4 Diagnostics and data treatment

Visible images were recorded to compare flame height, luminosity, attachment, oscillation, and overall morphology. A FLIR GF320 infrared camera was operated with a 240-400 °C display window to improve contrast. The infrared images are interpreted as relative maps of the flame contour and high-response region; they are not used as absolute gas-temperature measurements because emissivity, optical path length, and gas-band radiation vary among conditions.

Temperature was measured with K-type sheathed thermocouples at 0, 6.5, 13, 29, 45, and 61 cm relative to the nozzle reference position. For the free flame, the probes were on the centerline. For the metal fiber burner, the lower probes sampled the near-wall/near-field region and the upper probes sampled the plume. At 5 L/min the collection hood had to be lowered for reliable flue-gas capture and interfered with the 61 cm position; this point was therefore excluded rather than interpolated.

A TS-34C total heat-flux sensor was positioned approximately 0.75 m from the flame. CO and NOx were measured using an MGA6 plus analyzer from gas collected above the flame. Concentrations are reported on the analyzer dry basis. Because the apparatus is an open coflow system, small ambient-air entrainment and trace gas impurities can produce non-zero NOx even though the prepared oxidizer contains no nitrogen diluent. The principal measurement purposes are summarized in Table 4.

Table 4. Diagnostic instruments and analysis objectives.

Quantity	Instrument or model	Purpose
Visible flame image	Canon HG10 / visible camera	Flame height, luminosity, attachment, and stability
Infrared flame image	FLIR GF320	Relative flame contour, high-response region, and plume development
Temperature	KPS-IN600-K K-type sheathed thermocouple	Fixed-height thermal response
Radiative heat flux	TS-34C total heat-flux sensor	External radiative loading
CO and NOx	MGA6 plus flue-gas analyzer	Combustion efficiency and nitrogen-oxide response
Data acquisition	OM-DAQPRO-5300	Synchronous temperature and heat-flux acquisition

2.5 Quantitative indicators

Two normalized indicators were used to summarize oxygen-enrichment and load effects. The CO reduction ratio between 21% and 35% O_2 is defined as

$$\eta CO = (CO21 - CO35) / CO21 \times 100\%$$

and the heat-flux amplification between 5 and 20 L/min is

$$Rq = q20\ L/min\ /\ q5\ L/min\ .$$

Numerical values read from the processed plots are reported as approximate values to avoid implying precision beyond the graphical resolution. Trends are interpreted together with the flame images and fixed-position temperature measurements.

3. Results and discussion

The discussion follows the physical sequence from flame organization to thermal response, external radiation, and final emissions. This ordering is essential for O_2/CO_2 combustion because a lower visible luminosity can coexist with a substantial gas-radiation field, and a locally high thermocouple reading does not guarantee complete CO post-oxidation throughout the plume.

3.1 Flame morphology and combustion structure

3.1.1 Visible flame evolution

Fig. 2 presents the visible metal fiber burner flames. At 5 L/min the flame was short, predominantly blue, and concentrated near the cylindrical surface. The weak luminosity is consistent with CO_2 thermal dilution and limited soot-related radiation. Raising the methane flow to 10-20 L/min enlarged both the near-wall reaction region and the upper plume. A bright yellow-white region appeared at high load, showing that the increased chemical heat release and surface feedback could partially overcome the cooling effect of CO_2. Oxygen enrichment generally strengthened the plume, although the visual response was not proportional to oxygen fraction because the heat-release zone shifted spatially.

At a fixed oxygen fraction, the transition with methane flow rate is therefore more pronounced than the transition with oxygen fraction. The 5 L/min image represents a surface-dominated mode in which the luminous region occupies only part of the cylinder height and the upper plume is discontinuous. At 10 L/min, the reaction becomes spatially connected and a persistent plume appears. At 15 and 20 L/min, the plume dominates the visible field, but the blue base remains visible around the metal surface. This coexistence indicates that fuel continues to emerge over the sidewall while excess fuel and intermediate species are consumed above the cylinder.

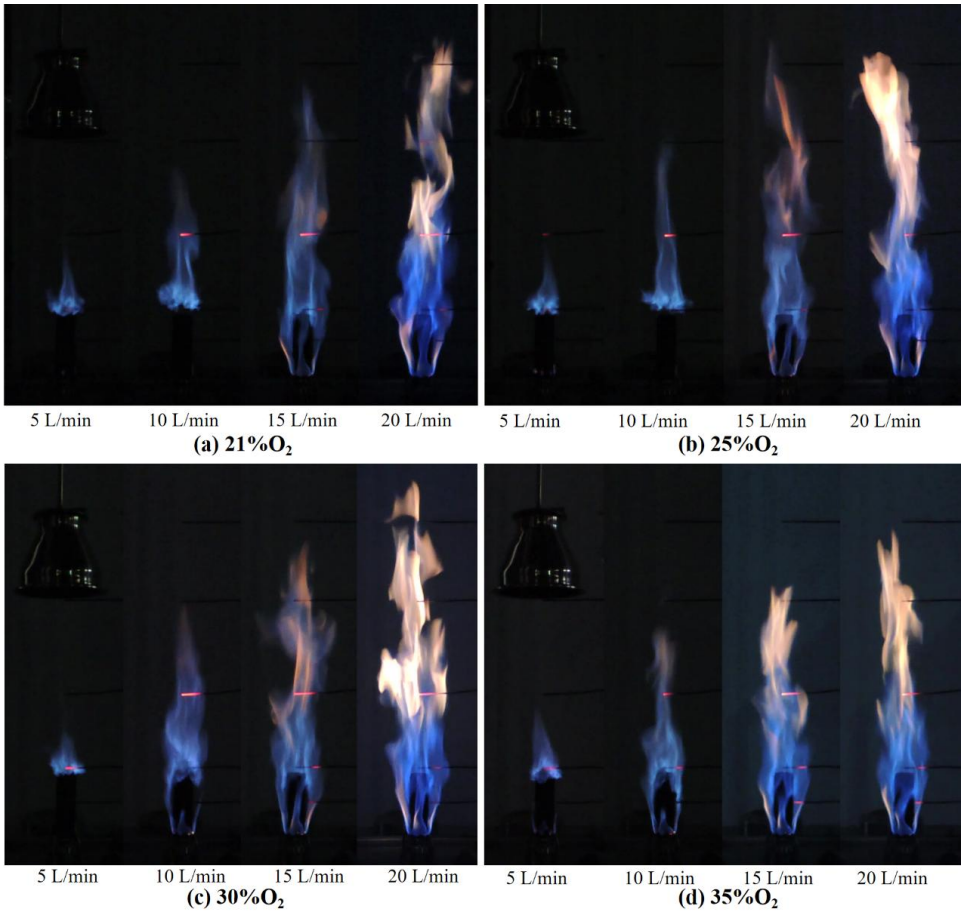


Fig. 2. Visible images of cylindrical metal fiber burner flames at different methane flow rates and oxygen fractions in O_2/CO_2.

The effect of oxygen enrichment is the most pronounced at 5-10 L/min, where the blue reaction region becomes more defined and the plume becomes less intermittent. At higher load, image saturation in the yellow-white plume limits direct luminosity comparison, so the temperature, radiation, and gas-analysis measurements provide a more reliable basis for quantification. The morphology is consistent with the sensitivity of non-premixed O_2/CO_2 flames to oxygen fraction reported by Kim et al. [8], but the present sidewall fuel distribution creates a surface-supported mode that is absent from a coaxial jet.

The weak visible output at low load should not be interpreted as poor flame anchoring. The flame remains attached to the porous surface, but the radiating-gas volume and

soot-precursor luminosity are small. CO_2 lowers the temperature of fuel-rich pockets and modifies the H/OH pool [9-11], while the metal matrix spreads heat away from individual micro-flames. The resulting blue flame is therefore a consequence of distributed oxidation and thermal dilution rather than imminent extinction alone.

The free diffusion flames in Fig. 3 retained the centerline jet structure. Flame height and oscillation amplitude increased with methane flow rate, and the upper reaction zone became more luminous at 15-20 L/min. The open jet generated a larger visible gas-phase post-flame region than the metal fiber burner, particularly at high load. At low load, however, both configurations retained a blue, weakly luminous signature, confirming that the CO_2-rich environment dominated flame morphology.

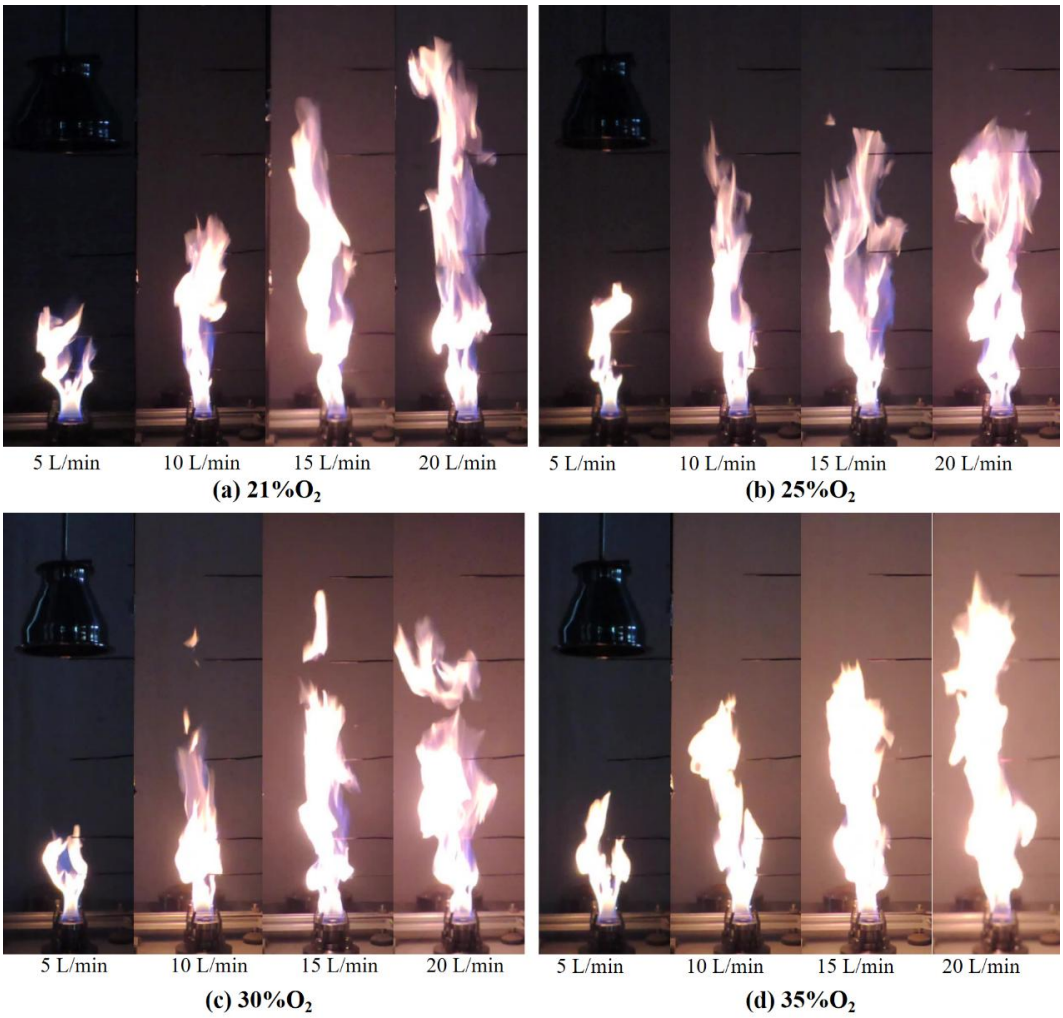


Fig. 3. Visible images of methane free diffusion flames at different methane flow rates and oxygen fractions in O_2/CO_2.

The free flame also provides a useful control for separating aerodynamic and material effects. Its fuel enters through the same 39 mm nozzle, so the total methane input is unchanged, but the fuel is divided among thousands of porous pathways. The centerline velocity and shear-layer entrainment therefore remain the dominant mixing mechanisms.

Oxygen enrichment affects both the local stoichiometric surface and the axial distance required for burnout. A higher oxygen fraction can shorten the fuel-rich core and intensify the outer reaction layer, yet the high CO_2 concentration continues to absorb sensible heat. The observed combination of a blue base and a yellow-white upper zone is consistent with a lower-temperature mixing layer feeding a hotter post-flame region. Similar oxy-methane porous-burner work has shown that oxygen fraction and internal heat recirculation jointly influence flame stabilization[25].

The images reveal that the cylindrical surface does more than shorten the flame. It changes the fuel boundary condition from a single central jet to multiple distributed micro-flows through the fibrous wall. The resulting reaction structure contains a surface-supported zone that exchanges heat with the solid matrix and a plume zone that is governed increasingly by gas-phase oxidation and buoyancy as fuel input rises. This distinction is central to interpreting the temperature and CO data.

3.1.2 Infrared response and plume development

The infrared images of the metal fiber burner (Fig. 4) show a clear response from the heated cylinder and the overlying plume. At 5 L/min the response was confined to the burner vicinity. At 10-20 L/min it expanded vertically and laterally, demonstrating that the high-load flame developed a larger radiating-gas volume. The cylinder response

confirms direct gas-solid heat exchange, but the images should not be read as absolute temperature maps.

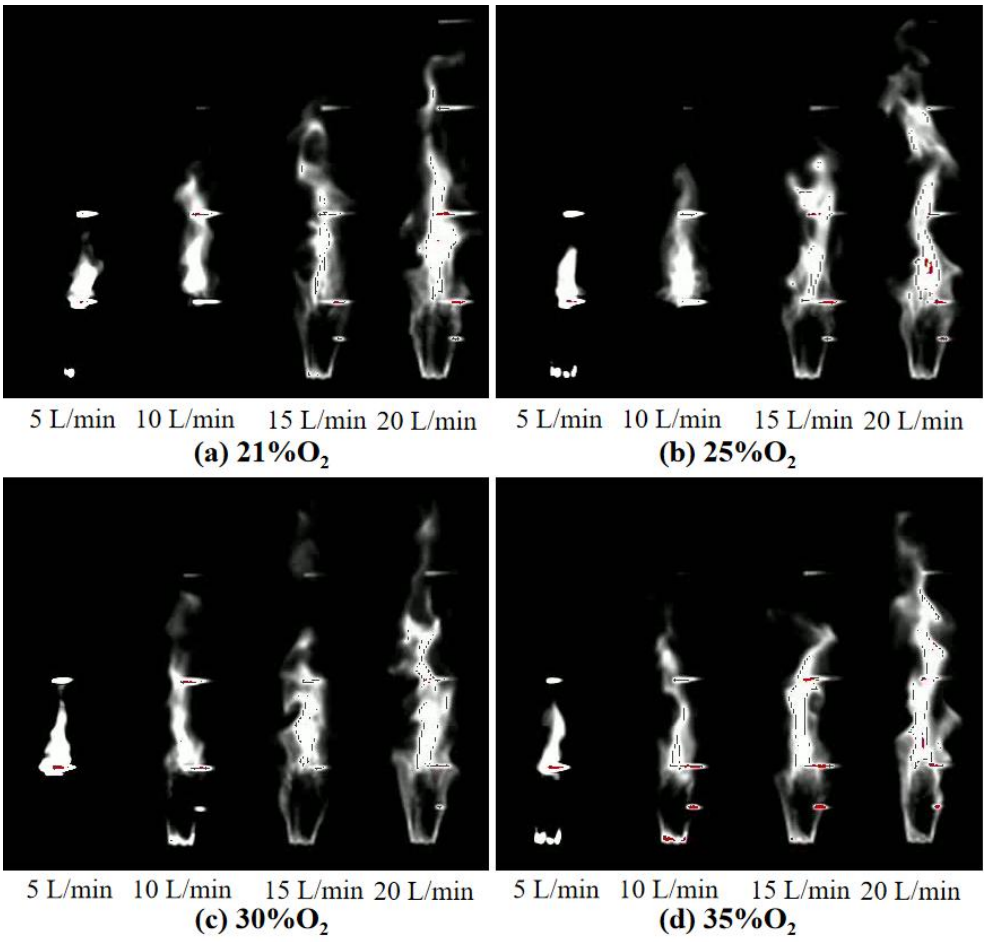


Fig. 4. Infrared images of cylindrical metal fiber burner flames in O_2/CO_2. The images indicate relative thermal structure rather than absolute gas temperature.

The infrared matrix further indicates that oxygen enrichment and fuel loading do not influence the thermal field in the same way. Increasing methane flow extends the plume and enlarges the emitting area, whereas increasing oxygen fraction mainly changes the intensity and compactness of the response at a given load. This distinction explains why methane flow rate later appears as the dominant variable for radiative heat flux.

The apparent response from the cylinder is produced by a combination of solid-surface emission and gas-band radiation along the optical path. Because the GF320 display window was fixed, comparisons are meaningful only as relative spatial patterns.

Nevertheless, the persistence of the cylinder response across the matrix confirms that the FeCrAl layer participates in the energy balance. This observation is consistent with experimental and numerical studies showing that metal fiber porosity and surface temperature influence both flame mode and emissions [17-23].

For the free flame (Fig. 5), the infrared response developed mainly along the centerline and broadened with methane flow. The upper part became increasingly dominant at high load. Comparison of Figs. 4 and 5 therefore identifies two thermal organizations: a surface-assisted distributed structure for the metal fiber burner and an axial gas-phase structure for the free flame. Both are strongly load dependent, but only the former influenced by a solid heat-storage and radiation.

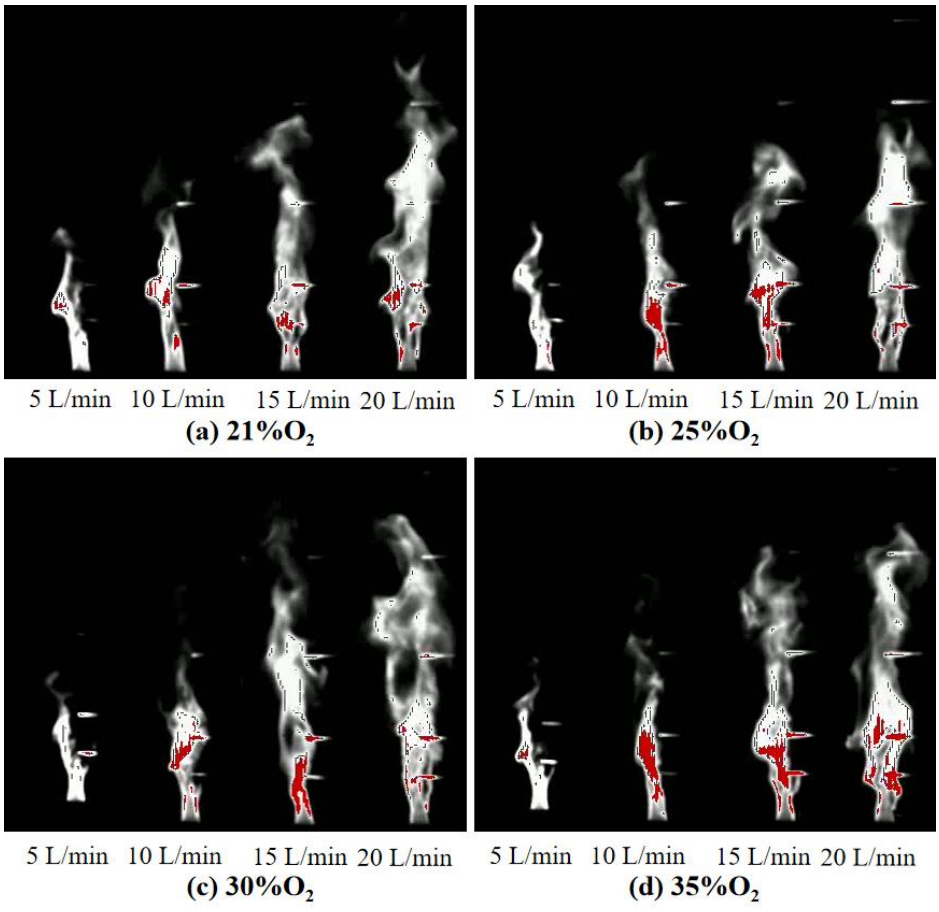


Fig. 5. Infrared images of methane free diffusion flames in O_2/CO_2.

At 5 L/min, the infrared response remains short even when the oxygen fraction reaches 35%, showing that increased oxygen cannot create a large radiating plume without

sufficient fuel heat release. At 20 L/min, by contrast, all oxygen fractions produce an extended response, and oxygen enrichment modifies the internal distribution rather than the existence of the plume. This load threshold is reflected consistently in the temperature and heat-flux results.

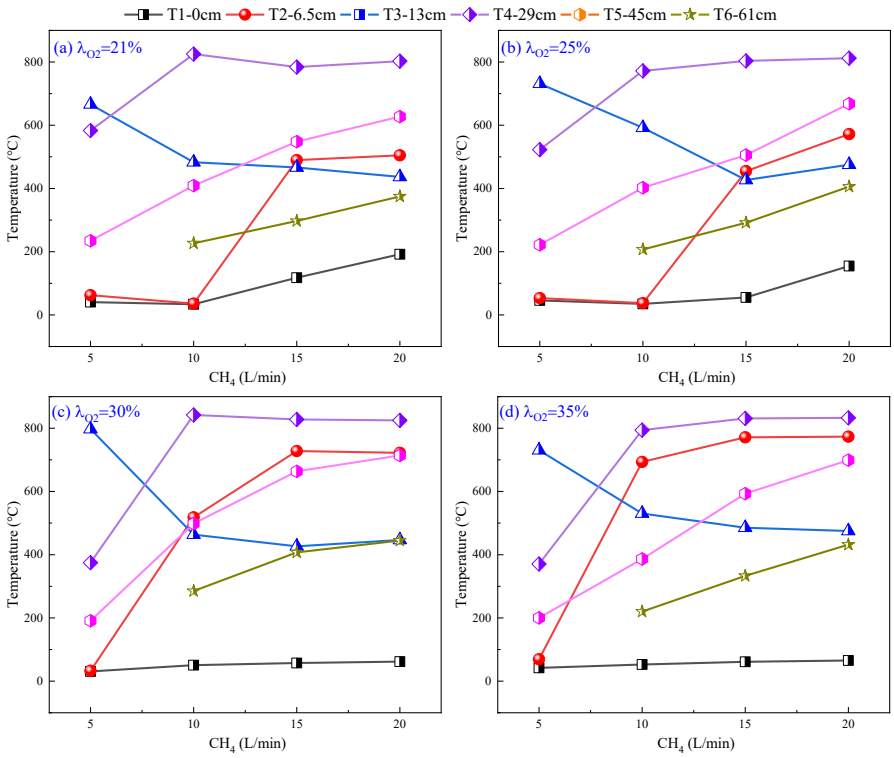
The thermal images also clarify why a single flame-height metric is insufficient. A higher plume contains a broad moderate-temperature region, whereas a shorter plume can contain a compact high-response core. The present analysis therefore combines images with six fixed-height thermocouples rather than assigning a single representative temperature to each condition.

Increasing oxygen fraction strengthened chemical oxidation, but the infrared response remained more sensitive to methane load than to oxygen fraction. The reason is that load controls total heat release, hot-gas volume, and plume persistence, whereas oxygen enrichment modifies reaction intensity within a plume whose overall size is still set primarily by fuel input. The subsequent temperature measurements test this image-based interpretation at fixed heights.

3.2 Temperature distribution and thermal response

3.2.1 Cylindrical metal fiber burner

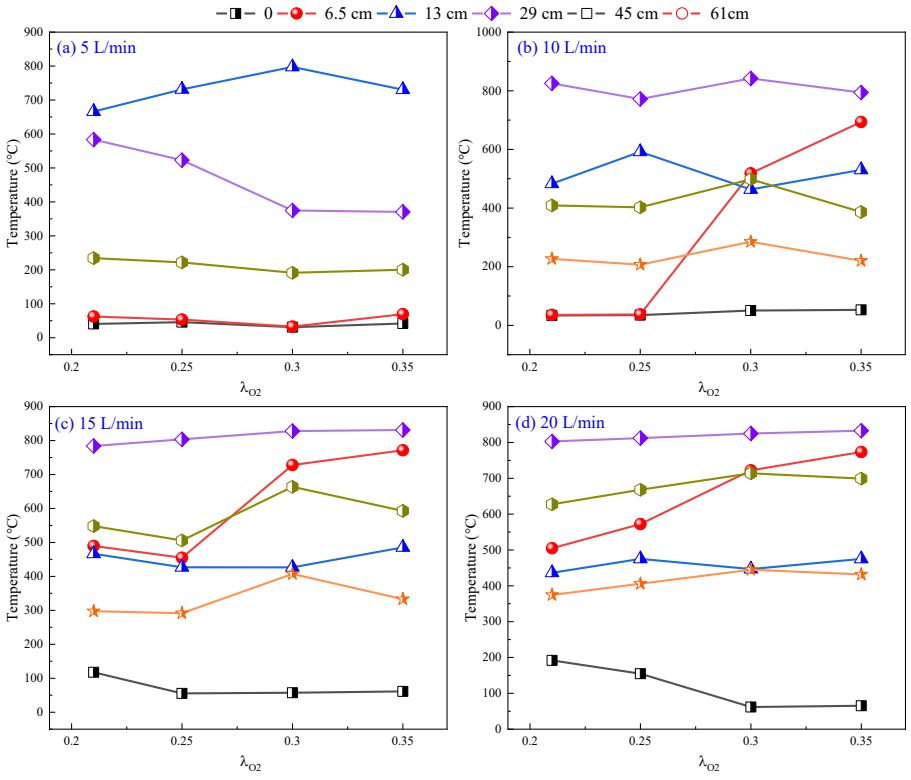
The temperature profiles of the metal fiber burner are shown in Figs. 6 and 7. The response was non-monotonic because that a fixed thermocouple could move relative to the reaction zone as flame height and plume width changed. Under several low-load conditions the 0 and 6.5 cm positions remained comparatively cool, demonstrating that the lower cylinder was not always the dominant heat-release region. The 13 and 29 cm probes more consistently sampled the near-field flame and upper plume, whereas the 45 and 61 cm probes represented upward heat transport.



296

297 **Fig. 6.** Temperature distribution of cylindrical metal fiber burner flames as a function

298 of methane flow rate in O_2/CO_2.



299

300 **Fig. 7.** Temperature distribution of cylindrical metal fiber burner flames as a function

301 of oxygen fraction in O_2/CO_2.

Methane flow rate produced the clearest thermal change. As the flow increased from 5 to 20 L/min, the high-temperature region extended upward and the 13-29 cm response strengthened. At high load, selected values in this region approached or exceeded approximately 800 °C. The result is consistent with the visible and infrared images: the weak surface flame at 5 L/min evolves into a fully developed surface/plume system after fuel input becomes sufficient to compensate for CO_2 dilution and solid heat loss.

The plotted profiles show that the increase is not uniform over height. The lower positions change modestly in several cases, while the 13 and 29 cm points rise sharply once the plume develops. This pattern implies that additional fuel does not simply heat the existing near-wall zone; it shifts a larger fraction of heat release into the gas phase above the cylinder. The 45 and 61 cm responses then increase because the hotter plume persists farther downstream.

At 5 L/min, the missing 61 cm value is methodological rather than physical. The collection hood was lowered to capture the small plume and interfered with the probe, so the point was excluded. Retaining it as zero or estimating it by interpolation would artificially steepen or flatten the profile. The exclusion is especially important when comparing load-dependent plume extension.

The high-load temperature level should also be interpreted as a sheathed-thermocouple response rather than the adiabatic flame temperature. Radiative loss from the bead, conduction along the sheath, finite response time, and local flame motion all bias the measured value. The approximately 800 °C values therefore quantify the relative thermal field at the probe locations and should not be used as equilibrium flame temperatures. The same diagnostic limitation applies to both configurations, allowing valid comparative interpretation.

The effect of oxygen fraction was less uniform. Raising O_2 increases the local reaction rate and supports CO oxidation, but the accompanying CO_2-rich medium still has a high thermal capacity and strong radiative activity. Moreover, enrichment can shift the reaction zone away from a given probe. Consequently, the temperature at each height did not increase synchronously from 21% to 35% O_2. This nonlinearity should not be interpreted as an absence of combustion enhancement; it reflects spatial redistribution of heat release in a participating-radiation medium.

For example, a probe may record a lower value after enrichment if the intensified reaction zone contracts or moves away from the thermocouple, even though total heat release and CO burnout improve. Conversely, a higher value at an upper probe can indicate plume migration rather than a uniform rise in the whole flame. The multi-height arrangement is therefore essential for distinguishing temperature magnitude from temperature-field position.

The response also reflects two-way coupling with the metal matrix. Gas-phase combustion heats the fiber surface, and the hot surface preheats newly emerging methane and the adjacent oxidizer. At the same time, axial conduction spreads energy toward cooler sections of the cylinder. Porous-burner modeling studies emphasize that local thermal non-equilibrium and effective conductivity strongly affect predicted flame position [26,27]; the present non-monotonic profiles provide experimental evidence of that sensitivity in a diffusion-mode metal fiber burner.

The lower-temperature response at 0-6.5 cm under low load also explains why the metal fiber burner can generate high CO. The solid matrix absorbs heat from a weak gas-phase reaction and transfers energy axially and radiatively. If chemical heat release is insufficient, the surface behaves partly as a heat sink, reducing the local OH-rich post-

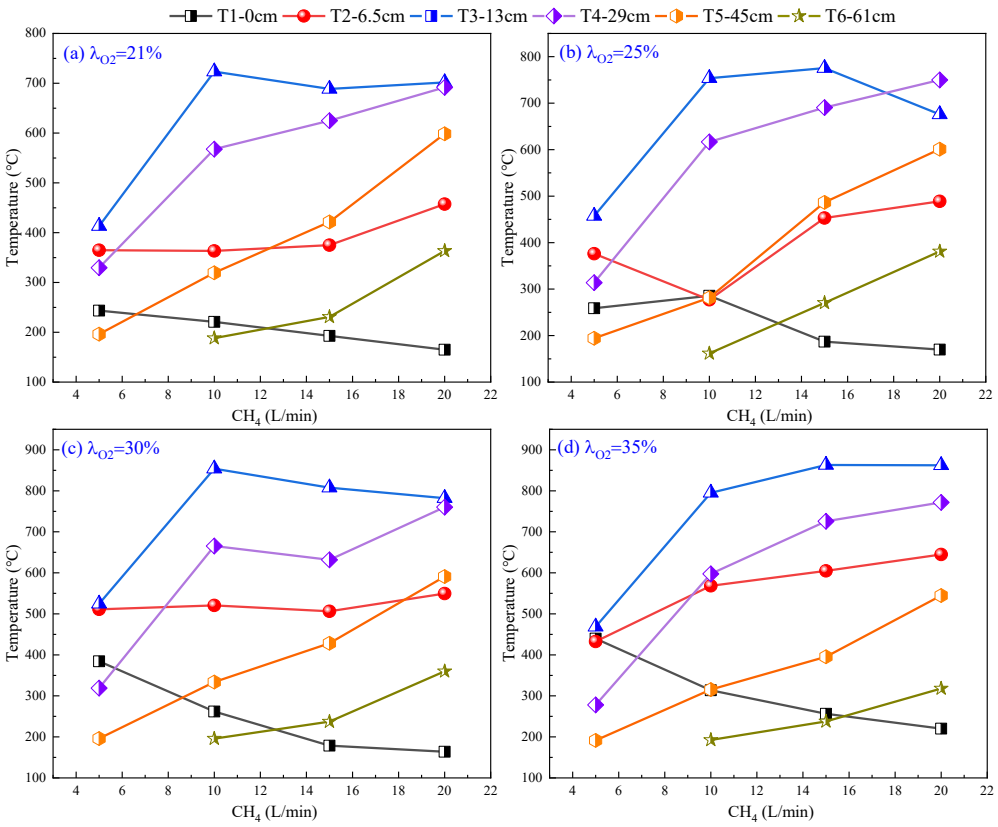
oxidation environment. At medium and high load, the direction of the balance changes: the hot matrix returns heat to the reaction zone and stabilizes the distributed flame.

3.2.2 Free diffusion flame

The free diffusion flame retained a predominantly axial temperature structure (Figs. 8 and 9). The 13 and 29 cm positions were generally the principal high-temperature locations. At 20 L/min their values approached the 800 °C level, consistent with the long thermal plume in Fig. 5. Increasing methane flow increased total heat release and jet momentum, moving the reaction and post-flame zones upward.

The separation between the 13-29 cm high-temperature region and the lower nozzle region is expected for a non-premixed flame with a large nozzle diameter. Fuel and oxidizer require a finite mixing distance before a substantial fraction of the methane reaches near-stoichiometric conditions. As flow rate rises, the mixing layer and buoyant plume lengthen, moving the maximum response upward. The visible images show the same trend, which confirms that the thermocouple profiles are tracking a real shift in flame structure rather than isolated fluctuations.

At the upper positions, temperature is governed by the competition between continued oxidation and dilution by entrained surrounding gas. Oxygen enrichment can extend oxidation farther downstream by reducing local oxygen deficiency, while CO_2 increases heat capacity and gas radiation. The observed profiles therefore combine chemical enhancement and enhanced energy loss, producing the measured nonlinear behavior.



370

371 **Fig. 8.** Temperature distribution of methane free diffusion flames as a function of
372 methane flow rate in O_2/CO_2.

373 Oxygen enrichment generally increased temperature and high-temperature persistence,
374 but again the response was not perfectly monotonic at every height (Fig. 9). The free
375 flame is mixing controlled; enrichment changes both the stoichiometric surface and the
376 axial position of the reaction zone. CO_2 simultaneously lowers the local adiabatic
377 temperature and redistributes radiation. The measured profile therefore represents the
378 intersection of an evolving flame with discrete probe locations rather than a single
379 global flame temperature.

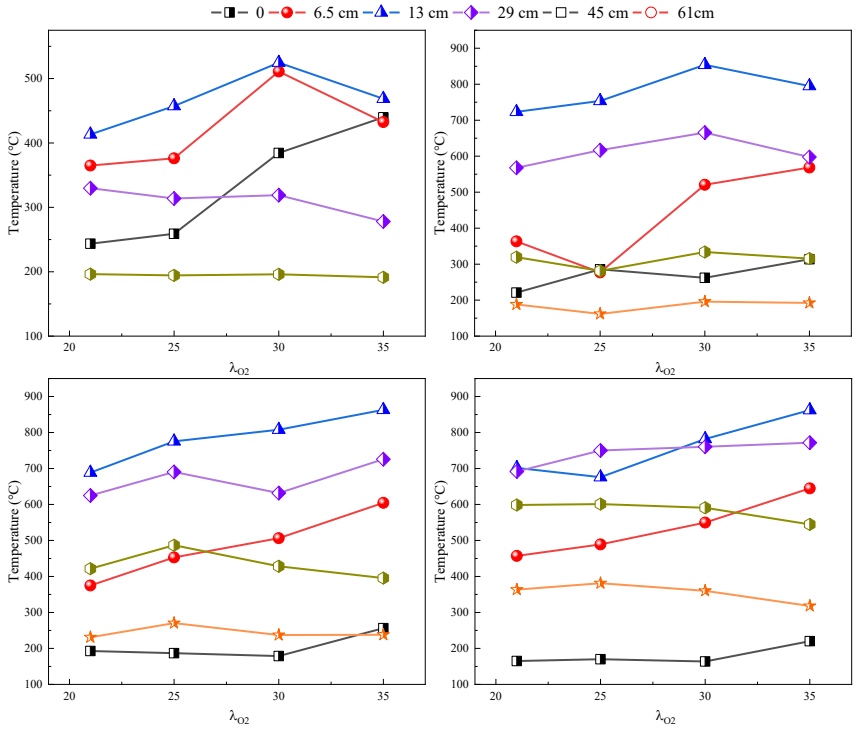


Fig. 9. Temperature distribution of methane free diffusion flames as a function of oxygen fraction in O_2/CO_2.

Compared with the metal fiber burner, the free flame avoids direct conductive loss to a porous surface. This difference is most important at 5-10 L/min, where free-flame CO is markedly lower. At higher load, both configurations develop broad hot plumes and the difference in combustion completeness narrows. Thus, the usefulness of the metal fiber matrix depends on whether its thermal feedback exceeds its heat-removal effect at the selected load.

The comparison also shows that the metal fiber burner does not universally increase measured temperature. Its benefit is spatial redistribution and potential surface stabilization, not guaranteed elevation of every fixed-point temperature. A design optimized only for maximum surface area can therefore increase low-load heat loss and CO. The preferred geometry should provide enough area for distributed mixing while limiting conduction to inactive parts of the cylinder.

3.3 Radiative heat-flux characteristics

Fig. 10 summarizes the radiative heat-flux response. Methane flow rate was the first-order control variable for both burner configurations. At 5 L/min the measured heat flux was approximately 35-50 W/m². At 20 L/min it increased to approximately 240-300 W/m², corresponding to an amplification factor of roughly 5-8 depending on oxygen fraction and configuration. The increase follows the rise in chemical energy input, radiating-gas volume, plume height, and exposed hot surface area.

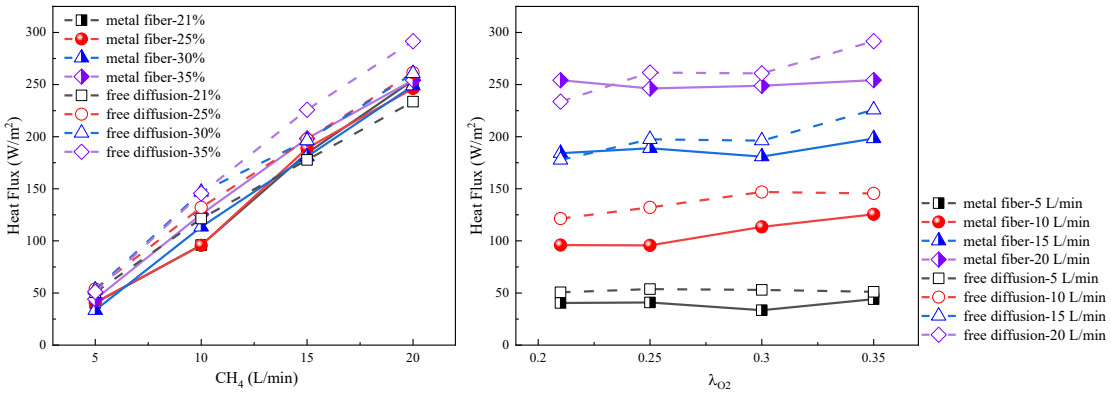


Fig. 10. Radiative heat flux as a function of methane flow rate and oxygen fraction in O_2/CO_2.

The slope of heat flux with methane flow is steepest between the low- and intermediate-load cases, where the flame changes from a compact near-field structure to a developed plume. Once the plume occupies the sensor view factor, further load increases raise temperature, emitting volume, and residence time simultaneously. This explains why a simple linear correlation with methane flow would not represent the full range accurately.

The metal fiber and free-flame curves converge more closely at high load than at low load. At low load, surface radiation from the heated matrix can make a relatively large contribution to the metal fiber signal, even though gas-phase combustion is weak. At high load, the large plume dominates both configurations and reduces the relative

importance of burner construction. The measured high-load range is therefore a property of the full flame-plume system rather than the metal surface alone.

Oxygen fraction provided a secondary amplification. Higher O_2 promotes reaction intensity and raises the temperature of CO_2/H_2O products, but the effect is moderated by heat-capacity dilution and flame-position changes. The metal fiber burner also adds solid-surface radiation. The measured flux can therefore be viewed qualitatively as the sum of gas-phase flame radiation, CO_2/H_2O band radiation, and radiation from the heated fibrous matrix.

CO_2 and H_2O have discrete emission bands, and their effective emissivity depends on temperature, partial pressure, and optical path length. Increasing methane load raises the production rate of both radiating species and expands the optical path through the plume. Oxygen enrichment can increase product temperature, but it also changes plume dimensions. The observed flux therefore represents an integrated radiative response rather than a direct proxy for any single thermocouple location [12,13].

For heat-utilization applications, this is beneficial: a CO_2-rich flame can transfer appreciable energy radiatively even when its visible luminosity is weak. For safety assessment, however, it means that visual inspection alone is unreliable. Thermal shielding and separation distances should be based on measured or modeled total heat flux.

The result has two engineering implications. First, weak visible luminosity at low load should not be extrapolated to high-load radiation safety. Once a sufficiently large hot plume is established, O_2/CO_2 combustion produces substantial external heat flux. Second, oxygen enrichment should be optimized together with fuel load, burner spacing, refractory protection, and exposure of nearby equipment. High-load

measurements, rather than the appearance of a low-load flame, should define the thermal design envelope.

3.4 Flue-gas composition and emissions

3.4.1 Load dependence

The load-dependent emission results are shown in Figs. 11 and 12. CO was highest at low methane flow, especially for the metal fiber burner. At 5 L/min its CO concentration was approximately 240-315 ppm, and at 10 L/min it was approximately 45-165 ppm. Increasing the flow to 15-20 L/min reduced CO to roughly 7-31 ppm. This strong decrease confirms that the low-load limitation is thermal and kinetic: higher fuel input enlarges the hot region, strengthens surface feedback, and increases residence time for $CO + OH \rightarrow CO_2 + H$.

The steep CO reduction with load is the clearest quantitative evidence of the transition from a heat-loss-dominated surface flame to a thermally self-supporting surface/plume system. Between 5 and 10 L/min, the metal fiber burner remains substantially higher in CO than the free flame, but the difference narrows as oxygen fraction rises. By 15-20 L/min, both configurations reach tens or single-digit ppm under the most oxygen-rich conditions.

CO concentration is an integrated indicator and is therefore more sensitive than a single temperature probe to incomplete oxidation over the full flame volume. The metal fiber burner can display a hot upper plume while still emitting CO generated in colder near-wall pockets. This explains why the CO curves should be interpreted together with both lower and upper temperature points.

The $CO_2 + H \rightleftharpoons CO + OH$ pathway can increase OH under some conditions, but the net effect depends on temperature and the competing consumption of H radicals. In the present low-load flames, thermal dilution and rapid cooling dominate, and the overall

CO-to-CO_2 conversion remains incomplete. Glarborg and Bentzen [9] and subsequent oxy-flame studies [10,11] similarly show that the chemical effect of CO_2 cannot be reproduced by heat-capacity matching alone.

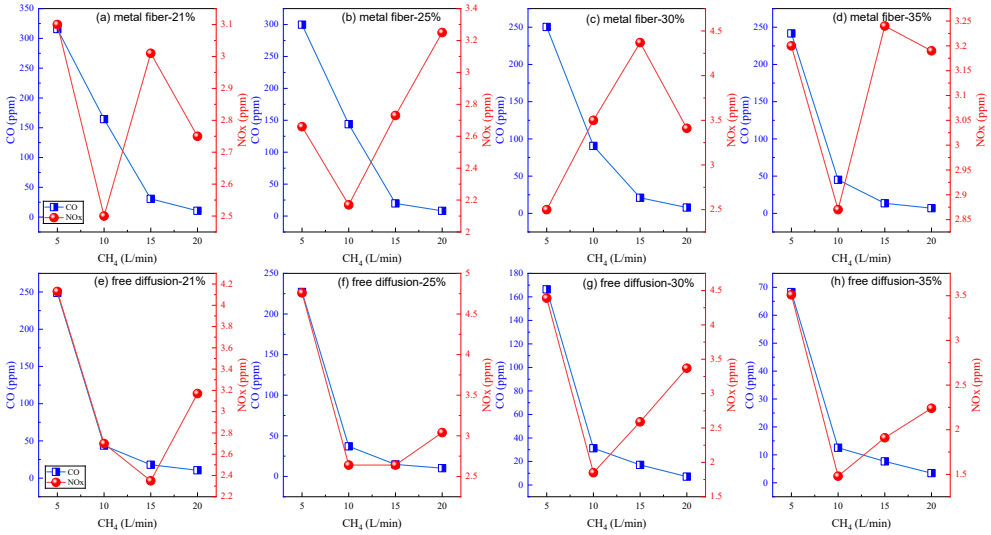


Fig. 11. Dry-basis flue-gas composition as a function of methane flow rate in O_2/CO_2.

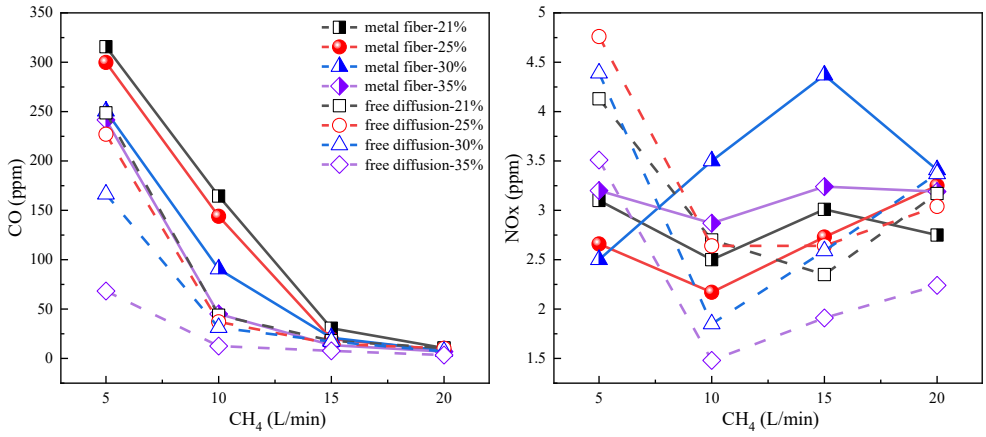


Fig. 12. Comparison of CO and NOx for free diffusion and cylindrical metal fiber burner flames in O_2/CO_2.

The free diffusion flame exhibited lower CO than the metal fiber burner at low load because it did not lose heat to the fibrous wall. Nevertheless, CO_2 dilution remained evident. The free-flame CO decreased approximately from 250 to 70 ppm at 5 L/min, from 43 to 12.5 ppm at 10 L/min, from 18 to about 7-8 ppm at 15 L/min, and from 10.5 to 3.5 ppm at 20 L/min as oxygen fraction increased. These values demonstrate that

oxygen availability remains effective for CO control, but the post-flame oxidation environment is still constrained by CO_2 thermal and chemical effects.

NOx remained approximately 1.5-4.8 ppm across most conditions. The low level reflects the absence of an intentional nitrogen diluent and the lower high-temperature peaks produced by CO_2. The residual signal is consistent with small ambient-air entrainment in the open apparatus, trace impurities, and analyzer background. Importantly, NOx did not show the rapid oxygen-enrichment penalty typical of nitrogen-containing oxidizers; the dominant practical emission constraint was CO burnout.

The weak dependence on load and oxygen fraction confirms that nitrogen availability, not oxygen availability, limits NOx formation in the tested system. The remaining variation is comparable to the sensitivity expected from small differences in air entrainment and sampling. Because the collection hood was positioned above an open flame, the measured values should be described as low-NOx rather than strictly zero-NOx.

This distinction is relevant for scale-up. A sealed oxy-fuel furnace with controlled leakage could reduce external nitrogen, but recycled flue gas, fuel-bound nitrogen, or seal leakage may reintroduce nitrogen species. The present data establish the burner-side baseline against which those system-level contributions can be evaluated [5-7].

3.4.2 Effect of oxygen fraction on CO

Figs. 13 and 14 isolate the effect of oxygen fraction. For the metal fiber burner, increasing O_2 from 21% to 35% reduced CO from approximately 315 to 240 ppm at 5 L/min, corresponding to $\eta CO \approx 24\%$. At 10 L/min, CO decreased from approximately 165 to 45 ppm, giving $\eta CO \approx 73\%$. The much larger reduction at 10 L/min shows that oxygen enrichment is most effective when thermal feedback and flame development

are already sufficient; at 5 L/min the near-wall heat-loss constraint prevents complete use of the added oxygen.

The contrast between the 5 and 10 L/min reduction ratios is particularly informative. At 5 L/min, additional oxygen cannot compensate fully for surface cooling, so the response is modest. At 10 L/min, the burner has crossed into a regime where the surface is sufficiently hot and added oxygen directly accelerates post-oxidation. For control purposes, the result suggests using a minimum thermal-state criterion before reducing methane load or CO_2-recycle temperature. If the surface or plume temperature falls below that criterion, localized secondary oxygen or temporary preheating may be more effective than increasing the bulk oxygen fraction of the entire coflow.

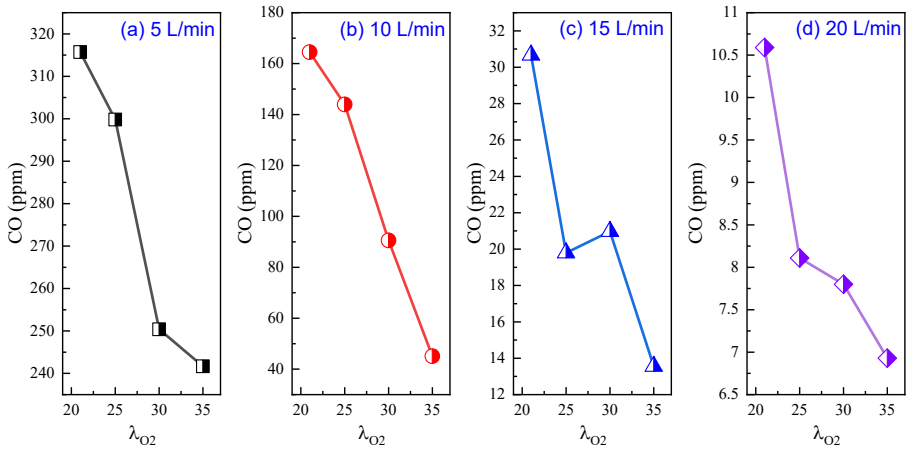


Fig. 13. CO variation with oxygen fraction for the cylindrical metal fiber burner in O_2/CO_2.

For the free flame, oxygen enrichment reduced CO over the entire load range (Fig. 14). The approximate 5 L/min decrease from 250 to 70 ppm corresponds to about 72%, while the 20 L/min decrease from 10.5 to 3.5 ppm corresponds to about 67%. The free flame therefore responds more directly at low load because the gas-phase reaction is not coupled to a cold porous surface. At high load, both configurations achieve comparatively low CO, although the free flame remains the cleaner of the two within the present geometry.

The difference between configurations is not evidence that the metal fiber concept is intrinsically inferior. The free flame achieves lower CO partly by maintaining all heat in the gas phase, but it lacks the distributed radiative surface and compact flame organization sought in many heating applications. The engineering decision is therefore a trade-off among CO, heat-transfer mode, flame footprint, and burner integration.

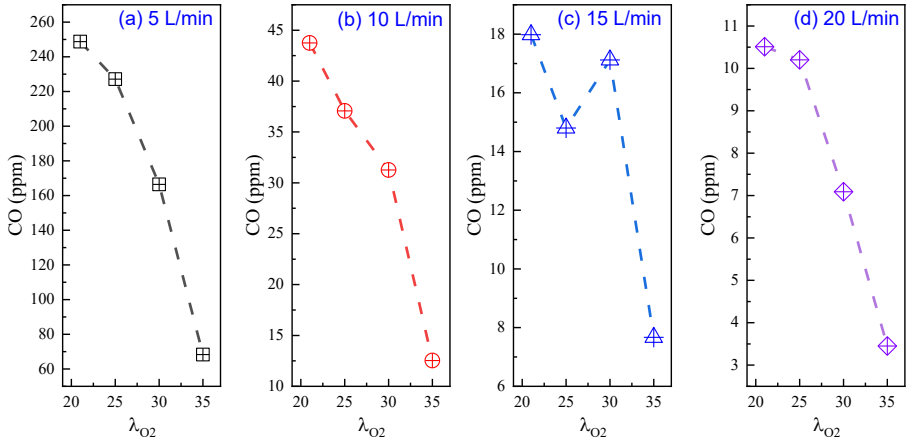


Fig. 14. CO variation with oxygen fraction for the free diffusion flame in O_2/CO_2.

The CO results show that oxygen fraction alone is not an adequate control variable. The same increase in O_2 produces a limited benefit when surface heat loss dominates and a large benefit when the thermal plume is developed. Burner control should therefore combine load, surface temperature or a surrogate thermal signal, and flue-gas CO rather than relying only on oxidizer composition.

3.4.3 NOx response

The metal fiber and free-flame NOx responses are presented in Figs. 15 and 16. Values remained within a narrow low-ppm envelope and showed only weak, non-monotonic changes with oxygen fraction. This behavior is expected because the prepared coflow contains no nitrogen reservoir for the extended Zeldovich mechanism. Oxygen enrichment may increase local temperature, but nitrogen availability remains the limiting factor.

The narrow range also shows that the large CO changes are not accompanied by an opposing NOx increase. This separates the present O_2/CO_2 system from nitrogen-containing enrichment strategies, where improved burnout may create a strong thermal-NOx penalty. In the tested matrix, oxygen fraction can therefore be used primarily as a CO-control variable, with radiation and material temperature providing the main upper constraints.

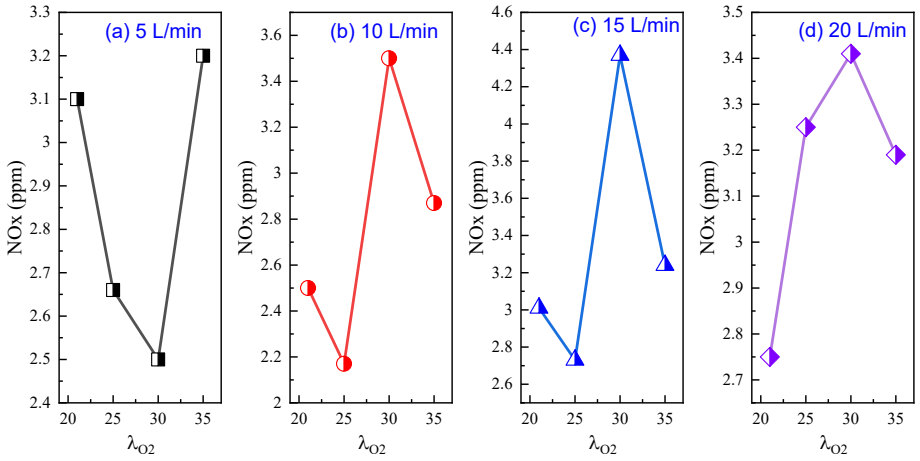


Fig. 15. NOx variation with oxygen fraction for the cylindrical metal fiber burner in O_2/CO_2.

The free flame showed the same qualitative behavior (Fig. 16). Small differences among flow rates can arise from ambient entrainment, plume length, collection efficiency, and local high-temperature residence. The measured envelope indicates that NOx control is an inherent advantage of the O_2/CO_2 route under the tested open-flame conditions. Further optimization should therefore target CO without sacrificing the CO_2-rich exhaust composition.

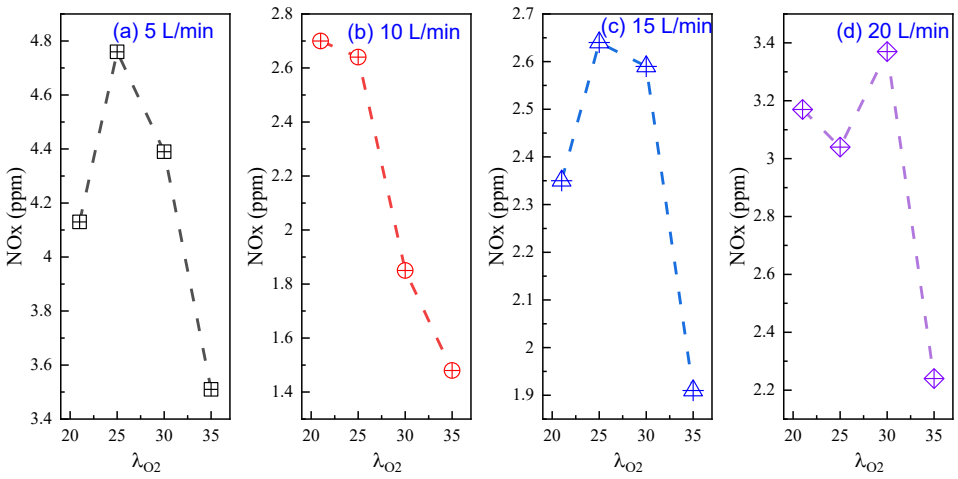


Fig. 16. NOx variation with oxygen fraction for the free diffusion flame in O_2/CO_2.

3.5 Integrated structure-thermal-radiation-emission mechanism

Fig. 17 integrates the measured responses. The O_2/CO_2 coflow controls oxygen availability while imposing CO_2 heat-capacity dilution, infrared participation, and radical-chemistry effects. The cylindrical metal fiber burner redistributes methane over the sidewall and introduces solid conduction and surface radiation. These two inputs generate the observed near-wall surface flame and upper plume. The resulting temperature field controls both the size of the radiating CO_2/H_2O volume and the OH-dependent CO post-oxidation pathway.

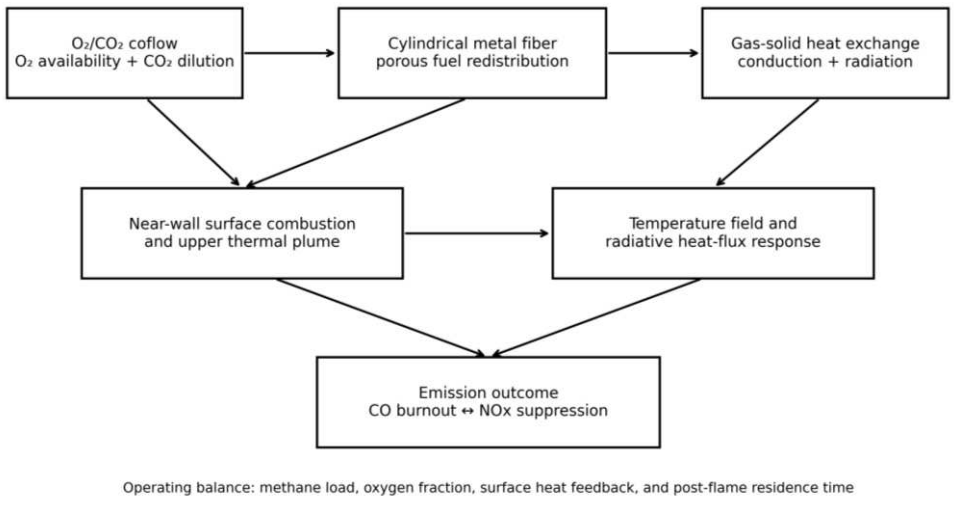


Fig. 17. Proposed structure-thermal-radiation-emission coupling mechanism for methane combustion with a cylindrical metal fiber burner in O_2/CO_2.

At low load, the near-wall flame is weak, the matrix removes a significant fraction of the released heat, and the post-flame zone is short. CO remains high even when oxygen fraction is increased. At medium load, surface heat feedback and the upper plume become mutually reinforcing; CO drops rapidly while NOx remains low. At high load, burnout is improved and radiative heat flux becomes the principal safety constraint. Thus, the system transitions from a CO-limited regime to a radiation-limited regime as methane flow increases.

Representative numerical ranges from the figures are consolidated in Table 5.

Table 5. Representative quantitative characteristics of the O_2/CO_2 flames.

Response	Cylindrical metal fiber burner	Free diffusion flame	Interpretation
Visible/infrared structure	Near-wall surface flame plus upper plume	Centerline jet flame plus axial plume	Burner configuration redistributes the reaction zone
High-temperature region	13-29 cm; approaches ~800 °C at high load	13-29 cm; approaches ~800 °C at 20 L/min	Methane load governs plume development
Radiative heat flux	~35-50 W/m² at 5 L/min; ~240-300 W/m² at 20 L/min	Comparable high-load range	Load dominates external thermal exposure
CO at 5 L/min	~315 to 240 ppm from 21% to 35% O_2	~250 to 70 ppm	Low-load wall cooling penalizes the metal fiber burner
CO at 10 L/min	~165 to 45 ppm	~43 to 12.5 ppm	Oxygen enrichment becomes more effective after plume development

NOx	Mostly ~1.5-4.8 ppm	Mostly ~1.5-4.8 ppm	Nitrogen availability is strongly restricted

4. Mechanistic interpretation and engineering implications

4.1 Coupled physical and chemical role of CO_2

CO_2 should not be described simply as an inert replacement for nitrogen. Its high heat capacity reduces local temperature and can slow the formation of OH radicals needed for CO oxidation. At the same time, CO_2 and the produced H_2O participate in infrared emission and absorption, redistributing heat between the plume, the metal surface, and the surroundings. The reaction $CO_2 + H \rightleftharpoons CO + OH$ further modifies the H/OH radical pool [10]. These effects explain the central result of the study: the O_2/CO_2 route maintains very low NOx, but low-load CO remains sensitive to the spatial temperature and residence-time history rather than to bulk oxygen fraction alone.

The fixed-height temperatures provide only local evidence, whereas CO integrates the entire oxidation history before sampling. A thermocouple can therefore record a high value near 13 or 29 cm while CO remains elevated because part of the plume bypasses an OH-rich post-flame zone or cools rapidly through radiation and entrainment. This distinction should guide interpretation of open oxy-fuel flames and argues for combined thermal and emissions monitoring.

4.2 Dual role of the metal fiber matrix

The metal fiber matrix has a load-dependent dual role. It improves fuel distribution and increases the surface area over which mixing occurs. Once heated, it returns energy by radiation and convection and stabilizes the near-wall reaction. These effects are beneficial at 10-20 L/min. At 5 L/min, however, the matrix can conduct and radiate away a large fraction of the limited heat release. The resulting low gas temperature and

600 short plume inhibit CO burnout. This explains why the free flame has lower CO at low
601 load even though the metal fiber burner offers a more distributed reaction surface.
602 Structural optimization should therefore aim to reduce cold-surface quenching without
603 creating excessive material temperature or pressure drop. Candidate measures include
604 axial zoning of permeability, local reduction of surface area near the inlet, controlled
605 preheating, staged or localized oxygen addition, and a short post-oxidation zone above
606 the cylinder. These measures should be assessed against high-load radiative exposure
607 and material limits rather than against CO alone.

608 **4.3 Engineering operating window**

609 The present data identify three practical regimes. In the low-load regime near 5 L/min,
610 NOx is already low but CO is several hundred ppm for the metal fiber burner; operation
611 requires enhanced surface feedback or secondary oxidation. In the intermediate regime
612 near 10-15 L/min, the surface/plume structure is developed, oxygen enrichment
613 substantially reduces CO, and radiative heat flux remains below the maximum
614 measured envelope. This is the preferred operating region for the tested geometry. At
615 20 L/min, CO is minimized and NOx remains low, but external radiation approaches
616 240-300 W/m² and becomes the controlling safety consideration. These regimes and
617 their recommended control priorities are summarized in Table 6.

618 **Table 6.** Engineering interpretation of the operating regimes for the tested burner.

Regime	Observed behavior	Primary constraint	Recommended control focus
Low load (5 L/min)	Weak surface flame; short plume; metal-fiber CO ~240-315 ppm	CO burnout and local quenching	Surface preheating, localized O_2, longer post-oxidation residence

Intermediate load (10-15 L/min)	Developed surface/plume structure; strong CO reduction with O_2	Balance of burnout and radiation	Closed-loop control using CO and thermal response
High load (20 L/min)	CO ~single to tens of ppm; NOx low; q ~240-300 W/m²	Radiative exposure and material temperature	Spacing, shielding, refractory protection, and load limits

Because the apparatus is open, the results should be translated cautiously to a sealed industrial furnace. A closed system would reduce ambient entrainment, increase CO_2 concentration, and change radiation path length and residence time. Nevertheless, the experimentally observed regime transition and the relative effects of methane load and oxygen fraction provide a direct basis for subsequent enclosed-burner design and scale-up.

5. Conclusions

(1) The cylindrical metal fiber burner redistributed methane through its porous sidewall and transformed the centerline jet flame into a coupled near-wall surface-combustion region and upper thermal plume.

(2) Methane flow rate was the dominant variable governing flame scale, fixed-height thermal response, and external radiation. The 13-29 cm region approached approximately 800 °C at high load, while radiative heat flux increased from about 35-50 W/m² at 5 L/min to 240-300 W/m² at 20 L/min.

(3) Oxygen enrichment improved CO burnout in the CO_2-rich atmosphere. For the metal fiber burner, CO decreased from approximately 315 to 240 ppm at 5 L/min and from 165 to 45 ppm at 10 L/min as O_2 increased from 21% to 35%. At 15-20 L/min, CO fell to approximately 7-31 ppm.

(4) NOx remained approximately 1.5-4.8 ppm across most conditions because the prepared oxidizer contained no nitrogen diluent and CO_2 moderated high-temperature NO formation. The principal emissions constraint was therefore low-load CO rather than NOx.

(5) The tested burner exhibits a load-dependent transition from a CO-limited low-load regime to a radiation-limited high-load regime. For this geometry, the intermediate 10-15 L/min range best exploits surface thermal feedback while avoiding the highest external heat flux.

Acknowledgment

This research was funded jointly by National Natural Science Foundation of China (Grant No. 52604412) and the Ministry of Science and Technology of China Petroleum and Chemical Corporation (No. 324002).

CRediT authorship contribution statement

Yujie Lin: Conceptualization, Methodology, Investigation, Writing - original draft, Funding acquisition.

Chang Qi: Investigation, Resources.

Chen Kuang: Formal analysis, Visualization.

Guanlin Peng: Investigation, Data curation.

References

[1] Toftegaard MB, Brix J, Jensen PA, Glarborg P, Jensen AD. Oxy-fuel combustion of solid fuels. Prog Energy Combust Sci 2010;36:581-625. https://doi.org/10.1016/j.pecs.2010.02.001.

[2] Scheffknecht G, Al-Makhadmeh L, Schnell U, Maier J. Oxy-fuel coal combustion - A review of the current state-of-the-art. Int J Greenh Gas Control 2011;5:S16-S35. https://doi.org/10.1016/j.ijggc.2011.05.020.

662 [3] Talei S, Fozer D, Varbanov PS, Szanyi A, Mizsey P. Oxyfuel combustion makes
663 carbon capture more efficient. ACS Omega 2024;9:3250-3261.
664 https://doi.org/10.1021/acsomega.3c05034.
665 [4] Hamdy M, Abdelhalim A, Haque MA, Abdelhafez A, Nemitallah MA. Flow,
666 combustion and species fields of premixed CH4/H2/CO syngas oxy-flames on a
667 swirl burner: Effects of syngas composition. Int J Hydrogen Energy
668 2024;68:1398-1411. https://doi.org/10.1016/j.ijhydene.2024.04.336.
669 [5] Sun Z, Wu Q, Zhao C, Li H, Zhang A. A review of NOx control by MILD-oxy
670 combustion. J Energy Inst 2024;113:101502.
671 https://doi.org/10.1016/j.joei.2023.101502.
672 [6] Wu H, An Z, Zhang K, Mao Y, Zheng Z, Liu Z. Experimental study on NOx
673 emission characteristics under oxy-fuel combustion. Clean Energy 2023;7:595-
674 601. https://doi.org/10.1093/ce/zkad007.
675 [7] Zhao Z, Zhang Z, Zha X, Gao G, Li X, Wu F, et al. Internal association between
676 combustion behavior and NOx emissions of pulverized coal MILD-oxy
677 combustion affected by adding H2O. Energy 2023;263:125878.
678 https://doi.org/10.1016/j.energy.2022.125878.
679 [8] Kim T, Bukar M, Basnet S, Magnotti G. Effects of O2 concentration of O2/CO2
680 co-flow on the flame stability of non-premixed coaxial jet flame. Fuel
681 2024;371:132114. https://doi.org/10.1016/j.fuel.2024.132114.
682 [9] Glarborg P, Bentzen LLB. Chemical effects of a high CO2 concentration in oxy-
683 fuel combustion of methane. Energy Fuels 2008;22:291-296.
684 https://doi.org/10.1021/ef7005854.

685 [10] Chen Y, Wang J, Zhang X, Li C. Comparisons of the uncoupled effects of CO2
686 on the CH4/O2 counterflow diffusion flame under high pressure. Appl Sci
687 2021;11:1768. https://doi.org/10.3390/app11041768.
688 [11] Fordoei EE, Mazaheri K, Mohammadpour A. Numerical study on the heat
689 transfer characteristics, flame structure, and pollutants emission in MILD
690 methane-air, oxygen-enriched and oxy-methane combustion. Energy
691 2021;218:119524. https://doi.org/10.1016/j.energy.2020.119524.
692 [12] Paulauskas R, Jancauskas A, Bykov E, Vorotinskiene L, Zakarauskas K.
693 Experimental study on luminescence and thermal radiation characteristics of
694 plasma-assisted biogas flames changing CO2 dilution level. Fuel
695 2024;371:132014. https://doi.org/10.1016/j.fuel.2024.132014.
696 [13] Kumuk O. CO2, Ar, and He dilution effects on combustion dynamics and
697 characteristics in a laboratory-scale combustor. Fuel 2024;369:131745.
698 https://doi.org/10.1016/j.fuel.2024.131745.
699 [14] Mujeebu MA, Abdullah MZ, Abu Bakar MZ, Mohamad AA, Abdullah MK.
700 Applications of porous media combustion technology - A review. Appl Energy
701 2009;86:1365-1375. https://doi.org/10.1016/j.apenergy.2009.01.017.
702 [15] Yu B, Kum SM, Lee CE, Lee S. Combustion characteristics and thermal
703 efficiency for premixed porous-media types of burners. Energy 2013;53:343-350.
704 https://doi.org/10.1016/j.energy.2013.02.035.
705 [16] Leonardi SA, Viskanta R, Gore JP. Analytical and experimental study of
706 combustion and heat transfer in submerged flame metal fiber burners/heaters. J
707 Heat Transfer 2003;125:118-125. https://doi.org/10.1115/1.1527910.

[17] Wang R, Qi B, Zhou Y, A R, Dong S. Numerical investigation on combustion and heating characteristics of metal fiber burner. Energies 2023;16:4301. https://doi.org/10.3390/en16114301.

[18] Wang T, Zhang Y, Zhang H, Lyu J. Stability and emissions of hydrogen-enriched methane flames on metal fiber surface burners. Int J Hydrogen Energy 2024;72:1308-1320. https://doi.org/10.1016/j.ijhydene.2024.05.465.

[19] Xu H, Wang B, Zhang Y, Ren R, Zhang G, Huang X. Combustion characteristics of low-concentration coal mine gas with metal fiber burners. Case Stud Therm Eng 2024;63:105256. https://doi.org/10.1016/j.csite.2024.105256.

[20] Azizi R, Farboud Z, Zabetian Targhi M. Efficient metal fiber burner characterization: chemiluminescence and image analysis. Energy 2025;333:137391. https://doi.org/10.1016/j.energy.2025.137391.

[21] Coskun G, Parlak Z, Yalcinkaya O, Pehlivan H, Tur V, Kosova O. Methane-fueled porous burner combustion in a domestic boiler: Experimental and numerical study. Fuel 2025;381:133391. https://doi.org/10.1016/j.fuel.2024.133391.

[22] Baghernavehsi H, Fazeli A. Comparison of conventional and metal fiber burners in a compact methane reformer using CFD modeling. Int J Hydrogen Energy 2023;48:28733-28746. https://doi.org/10.1016/j.ijhydene.2023.03.047.

[23] He C, Wang C, Li X, Li J, Chen D, Dong P, et al. Experimental and numerical study on surface combustion characteristics of a metal fiber burner using CH4/H2 blend fuels. Int J Hydrogen Energy 2026;234:155032. https://doi.org/10.1016/j.ijhydene.2026.155032.

[24] Munoz-Herrera C, Aravind B, Rojas P, Hernandez C, Mashruk S, Valera-Medina A, et al. Analysis of ammonia-methane stabilized flames in an optically accessible

porous media burner through chemiluminescence imaging. Fuel 2026;412:138122. https://doi.org/10.1016/j.fuel.2025.138122.

[25] Liao M, He Z, Jia S, Liang X, Chan TL, Li Y, et al. Comparison of the flame stabilities during oxy-methane and air-methane combustion in a two-layer porous burner. Case Stud Therm Eng 2023;51:103657. https://doi.org/10.1016/j.csite.2023.103657.

[26] Munoz-Herrera C, Skurtys O, Nikrityuk P, Hayes RE, Toledo M. Stabilization of methane-hydrogen flames inside a divergent porous media reactor. Proc Combust Inst 2024;40:105719. https://doi.org/10.1016/j.proci.2024.105719.

[27] Masset PA, Duchaine F, Pestre A, Selle L. Modelling challenges of volume-averaged combustion in inert porous media. Combust Flame 2023;251:112678. https://doi.org/10.1016/j.combustflame.2023.112678.

[28] Qi C, Ding J, Wang Y, Ning Y, Wang Y, Liang H, et al. Investigation of the upper flammability limit of ethylene/propane mixtures in air at high temperatures and pressures. Energy 2023;281:128114. https://doi.org/10.1016/j.energy.2023.128114.

[29] Qi C, Wang Y, Ning Y, Shi E, Yan X, Lv X, Yu J. Investigation on the upper flammability limits of ethylene/air and propane/air mixtures at high temperature and pressure. J Energy Inst 2023;109:101291. https://doi.org/10.1016/j.joei.2023.101291.

[30] Qi C, Yu X, Wang Y, Chen L, Yan X, Lv X, Liang H, Yu J. Investigating the effect of temperature, pressure, and inert gas on the flammability range of ethane/oxygen mixtures. Fuel 2023;354:129296. https://doi.org/10.1016/j.fuel.2023.129296.